Synthesis of laser-patterned MoS₂ nanoneedles for advanced electrochemical sensing

Pratik Joshi¹, Shubhangi Shukla², Siddharth Gupta³, Naveen Joshi¹, Jagdish Narayan¹, Roger Narayan¹,*

¹ Department of Materials Science and Engineering, North Carolina State University, Raleigh, NC 27695-7907, USA

²Joint Department of Biomedical Engineering, North Carolina State University, Raleigh, NC 27695-7907, USA

³ Intel Corporation, Rolner Acres Campus 3, OR, 97124, USA

*Corresponding Author E-mail: narayan@ncsu.edu (Jagdish Narayan), rjnaraya@ncsu.edu (Roger Narayan)

Abstract

We describe a novel excimer laser-based route for the fabrication of crystalline MoS₂ nanoneedles. Laser annealing of MoS₂

thin films at a low energy density of 0.08 Jcm⁻² resulted in a closed-pack structure with low defects and excellent

conductivity due to melting and rapid quenching. A further increase in laser annealing energy density resulted in the

formation of MoS₂ nano-needles. This structure of MoS₂ was found to have a remarkable reduction ability for H₂O₂ at -0.14

V over a wide linear range; a low detection limit (0.45 nM (S/N = 3)) and sensitivity of 2.38 μA/mM cm⁻² were

demonstrated.

Keywords: laser annealing, laser-induced reaction, nanostructure, sensor

1

I. Introduction

Transition metal dichalcogenides (TMDs) are being considered as a potential alternative to graphene due to their unusual properties such as high thermal conductivity, good spin-orbit coupling, superconductivity, high electron mobility, high charge-density-wave transition, excellent catalytic properties, and good biocompatibility [1–7]. MoS₂ (Point group: 6/mmm) is a member of this family with immense potential for advanced sensing applications owing to its direct band-gap (E_g=1.77eV, DFT calculated) with decreasing thickness of layers as opposed to the indirect band-gap (E_g=0.88eV, DFT calculated) behavior of the bulk crystal [8,9]. MoS₂-based nanostructures may be functionalized to detect proteins, DNA, cancer cells, and cell metabolism products such as H₂O₂ [10].

MoS₂ can be synthesized via either a top-down or bottom-up approach. The top-down approach involves mechanical, chemical, or electrochemical exfoliation. The bottom-up approach provides thin layers of MoS₂ and involves techniques such as metal-organic chemical vapor deposition, chemical vapor deposition (CVD), and molecular beam epitaxy (MBE) [11–15]. Pulsed laser deposition is a preferred method for the deposition of complex stoichiometric thin films. Conventional CVD processes require the maintenance of a specific gas ratio to obtain stochiometric films; the stoichiometry is easily disturbed with small variations in gas flow and temperature [16]. The efficacy of MoS₂ films for sensing depends on the crystallinity and the defects in the materials. Post-annealing of MoS₂ thin films may result in improved optical, bio-sensing, and electrical properties; the improvement is mostly associated with the elimination of amorphous clusters present in the MoS₂ thin films [17, 18]. A considerable amount of work has been carried out to study the effects of annealing atmosphere and duration on the properties of MoS₂ films. However, previous studies have not addressed the effect of excimer laser irradiation on the morphology and sensing properties of MoS₂ films [17,18].

The shape and size of MoS₂ structures influence the sensing functionality of these materials [19]. As such, it is important to explore the nanostructure of MoS₂ materials for sensing applications[20–26]. In this study, MoS₂ films deposited using pulsed laser deposition were laser annealed at energy densities of 0.08-0.4 Jcm⁻². The effect of laser annealing on the structural properties of MoS₂ thin films was evaluated using techniques such as scanning electron microscopy (SEM), transmission electron microscopy (TEM), and Raman spectroscopy; the electrochemical behavior of the MoS₂ films was also evaluated.

II. Experimental methods

The MoS₂ films were fabricated via pulsed laser deposition (PLD) on a Si (111) substrate and a subsequent laser annealing (LA) process as depicted in **Fig. 1**. The fabricated samples were evaluated using high-resolution scanning electron microscopy with electron backscatter diffraction capability, Raman spectroscopy, X-ray photoelectron spectroscopy (XPS), X-Ray diffraction, and transmission electron microscopy; cyclic voltametric measurements were performed to determine the H_2O_2 sensing behavior of the films. Additional details have been provided in the supplementary section.

III. Results and discussion

i. Imaging of the MoS₂ films

The threshold energy required for surface melting was estimated to be 50 mJ-cm⁻² by using the relationship $E_{th} = \frac{K\Delta T \tau^{0.5}}{(1-R_L)D^{0.5}}$. In this equation, ΔT is the difference between the melting temperature and substrate temperature of MoS₂, R_L is the reflectivity (=0.64), and D is the thermal diffusivity [27]. **Fig. 2 (a)** shows the SEM image of the as-deposited and MoS₂ thin film that was laser annealed at 0.08 Jcm⁻². The bright-colored laser-annealed region has melted; the as-deposited MoS₂ appears relatively dark in color. **Fig. 2 (b)** shows the 2D AFM image of MoS₂ laser annealed at 0.08 Jcm⁻². The MoS₂ formed at this energy density has a flat morphology without a globular or needle morphology.

Notably, AFM analysis showed that the MoS₂ film that was laser irradiated at 0.25 Jcm⁻² exhibited a globular morphology (**Fig. 2(c)**). SEM analysis, obtained by tilting the sample, revealed a needle-like morphology (**Fig. 2(d)**). The morphology is ideal for electrochemical sensing applications as it exposes the highly reactive MoS₂ planes. The crystalline nature of the MoS₂ needles was confirmed using the electron backscattered diffraction pattern data. Increasing the energy density to 0.4 Jcm⁻² resulted in a non-homogeneous film morphology, suggesting that the energy density was sufficient for MoS₂ film dissociation and sublimation. This result may also be due to the formation of MoO₃ and high film stresses.

Table 1 shows the dimensions of all of the MoS₂ coated Si samples used as working electrodes. These dimensions were extracted from both SEM and AFM data for these samples. Notably, the MoS₂ nanoneedles sample (E₃) exhibited a bimodal needle distribution; the distributions are termed as "1" and "2" respectively. The greater height of the grown needles as compared to the thickness can be attributed to the redistribution of material due to melting and solidification of the as-

deposited film after laser annealing. As previously mentioned, sample E₄ exhibited a non-uniform structure and hence could not be readily characterized.

Table 1. Summary of MoS₂ microstructural dimensions measured on MoS₂ coated Si electrodes; here, t, h, and w represent thickness, height and width of synthesized MoS₂ structures, respectively.

Electrode material	Processing	Dimensions (nm)
E ₁ (MoS ₂ on Si)	As deposited using PLD	t =52±5
E ₂ (LA MoS ₂ on Si)	LA at 0.08 Jcm ⁻²	$t = 40 \pm 2$
E ₃ (LA MoS ₂ on Si)	LA at 0.25 Jcm ⁻²	Distribution 1
		h~100; w=33±8
		<u>Distribution 2</u>
		h~1000; w=150±20
E ₄ (LA MoS ₂ on Si)	LA at 0.4 Jcm ⁻²	Inhomogeneous

ii. Defect and structural characterization

2H phase MoS₂ exhibits diffraction peaks centered at 14.5°, 33.69°, and 59.51°, corresponding to (002), (100), (103), and (110) planes. The XRD of non-annealed MoS₂ showed an amorphous nature with significant disorder (**Fig. 3(a)**). After laser annealing, the crystal planes were indexed to a = 0.3161 nm, b = 0.3161 nm, and c = 1.2299 nm (PDF card #01–071–9809) (**Fig. 3(b)**).

The laser annealed MoS₂ exhibited E^1_{2g} and A_{1g} modes, which originate from in-plane and out-of-plane vibrations. The (E_{2g}) breathing mode is located at ~383 cm⁻¹; an out-of-plane (A_{1g}) mode is located at 407 cm⁻¹. The MoS₂ film is characterized by an A_{1g} shift to higher frequencies and an E_{2g} shift to lower frequencies. The E_{2g} peak was observed at 379 cm⁻¹ and the A_{1g} peak was observed at 406.37 cm⁻¹ for the laser-annealed MoS₂ at 0.08 Jcm⁻². We observed a frequency shift (Δf) of 27.2 cm⁻¹ between the A_{1g} and E_{2g} mode. This shift is associated with bulk MoS₂ phase formation and the presence of more than five layers [18]. The as-deposited MoS₂ had a mostly amorphous structure with the presence of nanocrystalline islands. Hence, the Raman spectra showed the presence of peaks with high full-width half maxima (FWHM) and small variations in the FWHM value. In contrast, the laser annealed MoS₂ showed a uniform crystalline structure over the entire annealed region **Fig. 3(c)**.

The oxidation state of Mo in MoS_2 is +4. The Mo spectra are characterized by a doublet Mo $_{d3/2}$ and $Mo_{d5/2}$ at binding energies of ~233 and 230 eV. Two peaks of S were observed at 161.58 and 162.78 eV. Interestingly, the oxygen content of

~17% in as-deposited MoS₂ dropped to a mere 7% in laser-annealed MoS₂. The XPS spectra obtained from MoS₂ films before and after laser annealing is depicted in **Fig. S1**.

The selected area diffraction pattern acquired using transmission electron microscopy for laser annealed MoS2 was indexed along [100] zone axes (**Fig. 4(a)**). As indicated in **Fig. 4(b)**, the measured distance between the two {100} lattice fringes was ~0.27 nm. The sheet resistivity of the as-deposited MoS₂ was 80 k Ω , which was reduced to 6 k Ω after laser annealing at 0.08 Jcm⁻²; it should be noted that the sheet resistivity of the silicon substrate was measured to be 34 k Ω . The sheet resistivity measurements confirm the improvement in crystallinity after laser annealing.

iii. Electrochemical behavior of MoS₂ films fabricated using various laser parameters

Fig. 4a-d shows the polarization curves for as-deposited (E₁) and laser-annealed MoS₂ electrodes (referred to as E₂, E₃, E₄) that were processed at energy densities of 0.08, 0.26, and 0.4 Jcm⁻². The H₂O₂ reduction voltammograms of MoS₂-coated Si wafer electrodes were recorded in 0.5 M PBS (pH 7.2) containing 0.1 M KCl using serially diluted concentrations of H₂O₂ (0.30 nM - 52 mM) at a scan rate of 30 mV s⁻¹ over the potential window of -0.2 - 0.3 V. The CV curves (Fig. 5a) for electrode E₁ did not show a significant rise in cathodic current, with almost negligible electrochemical reduction of H₂O₂. However, a non-linear increase in anodic current was observed, owing to the presence of oxygen in the as-deposited MoS₂ film as indicated by the XPS profile (**Table S1**). The laser annealed electrode E₂ showed an apparent increase in cathodic peak current of $\sim 0.629 \,\mu\text{A}$ with a 9.1 nM H₂O₂ solution (Fig. 5b). Further amplification in the current component was recorded at approximately -0.17 V upon consecutive addition of H₂O₂. As compared to the E₂ electrode, the E₃ electrode showed a significant increase in the CV current even at a lower H₂O₂ concentration due to the larger surface area of the 2D MoS₂ films. As shown in the corresponding calibration plot, the rise in faradic current was proportional to the series of H₂O₂ additions (Fig. 5e-f). In contrast to the E₂ and E₃ MoS₂ films, the reduction peak currents for the E₄ film were exceptionally low (Fig. 5d). The subsequent calibration curves for E₂ and E₃ films exhibited a wide linear detection range from 0.3 nM to 52.1 mM; these values were broader than those of the E₁ and E₄ films, respectively. The slopes for different regions of electrodes E₂ and E₃ are closer, which define the linearity over a wide range of concentrations. The sensitivity for E₂ and E₃ MoS₂ films were calculated as 0.568 mA mM cm⁻² and 2.38 mA mM cm⁻², respectively, and the detection limits for E₂ and E₃ MoS₂ films were determined as 7.95 nM and 0.45 nM, respectively, at a signal-to-noise ratio of 3; these values were higher than those for the as-deposited film (E₁) and the film modified with an elevated energy densities (E₄). Therefore,

MoS₂ nanofilms deposited at 0.26 Jcm⁻² exhibited the highest sensitivity and lowest detection limit for electrochemical H₂O₂ reduction.

The laser-annealed films developed needle-like surface structures with an increasing energy density (0.08 – 0.26 Jcm⁻²), which are responsible for an enhancement in the surface area available for electrocatalysis. However, a further enhancement in energy density led to evaporation of the film (the nanoneedles formed by melting), which subsequently disrupted the stability of current flow and lowered the catalytic performance. Further, the reaction kinetics was analyzed by recording voltammograms at different scan rates (2 to 200 mV/s) using 2.5 mM H₂O₂ in 0.1 M PBS. There was a linear advancement in the current components for the E₃ system as shown in **Fig. 5 g-h**; the rest of the electrodes (E₁, E₂, and E₄) exhibited a feeble increase in current along with a nonlinear correlation for different scan rates (**Fig. S2, S3**). Using the current vs. scan rate plot, the diffusion coefficient was determined using the Randles-Sevcik equation:

$$Ip = 2.69 \times 10^5 n_2^3 AD_2^1 Cv_2^1$$
 (1)

In this equation, n is the number of electrons involved in the reaction, I_p is the peak current in A, C is the concentration in mol/cm³, D is the diffusion coefficient in cm²/s, V is the scan rate in V/s, and A is the electrode area in cm². The value D for E_3 was calculated as ~10⁻⁴ cm²/s, which was higher than those for E_1 , E_2 , and E_4 ; the reduction process was found to be diffusion controlled on E_3 . Furthermore, the catalytic activity of electrodes was studied in terms of effective electrochemical surface area (ECSA); it was estimated using the relation (2):

$$ECSA = Cdl/Cs (2)$$

In this equation, C_{dl} and C_s are double layers and specific capacitances, respectively. The cyclic voltammograms at different sweep speeds (2–200 mV s⁻¹) for E_3 (shown in **Fig. 4g**) were used to calculate C_{dl} (0.2125 mF), which equals half the value of slope (-0.425) from the calibration plot (Fig. 5h). Further, the specific capacitance (C_s) was calculated using the relation (3):

$$Cs = A/2km\Delta V \tag{3}$$

where A is the area under a particular I-V curve, k is the scan rate, m is the active mass of film – mass dipped in electrolyte, and ΔV is the potential window. For the E₃ electrode, the Cs was calculated to be 2.55 mFcm⁻². Further, the ECSA was determined to be 0.083 cm⁻².

For the commercial-scale applicability of this work, repeatability of the experiments is crucial. The reliability of the samples was confirmed by conducting multiple H_2O_2 sensing and microstructure characterization experiments using newly prepared samples, one month after the first set of experiments. The thin and uniform MoS_2 film deposited by pulsed laser deposition exhibited reproducible properties upon laser annealing with single laser pulse, indicating the complete conversion of amorphous clusters to crystalline. The evenness of the laser annealed MoS_2 films at 0.08 Jcm⁻² can be attributed to the consistency in the melt front during regrowth. The aspect ratio of needles formed by LA at 0.25 Jcm⁻² was ~7 for larger needles and as large as 30 for smaller needles. This ratio is similar to needle like nanodiamonds obtained by laser annealing in previous studies reported by the authors [28].

Table 2: Comparison of MoS_2 2D film-based electrochemical H_2O_2 sensing with other nanoscale sensors reported in the literature.

Working electrode	Potential (vs Ag/AgCl) V	Sensitivity	Concentration Range	LOD	Ref
MoS_2 nanofilm 0.26 Jcm^{-2} (E ₃)	-0.14	$2.38 \mu\text{A/mM cm}^{-2}$	0.30 nM – 52 mM	0.45 nM	this work
MoS_2 nanofilm 0.1 $Jcm^{-2}(E_2)$	-0.17	$0.568~\mu\text{A/mM cm}^{-2}$	0.30 nM – 52 mM	7.95 nM	this work
MoS ₂ microfiber	-0.3	-	$0.1-90~(\mu M)$	30 nM	29
MoS_2QDs	-0.46	-	0.01–5.57 mM	1.90 μΜ	30
MoS ₂ /PtNPs/AN	0.15	-	1 to 100 mM	0.686 μΜ	31
Layered Mb/MoS ₂ - GR	0.17	-	6.25–225 μΜ	1.25 μΜ,	32
MoS ₂ /PtNPs nanohybrids	-0.35	-	0.02 to 4.72 mM	0.345 mM	33
Au–MoS ₂ /HRP hybrid	-0.8	-	0 – 20 ng mL^{-1}	5 ng	34

Au@PBA(Ni– Fe):MoS ₂	0.0	-	0.5–3000 μΜ	0.23 mM	35
PtW/MoS ₂	-0.25	1.71 μ A /μ M c m ⁻²	1 μM -0.2 mM	5 nM	36
MoS ₂ -PBNCs	-0.3	-	0.005 - 10 ng mL^{-1}	$0.54~\mathrm{pg~mL^{-1}}$	37
Nafion/Hb/MoS ₂ /GC	0.1	-	$20-180~\mu ML^{-1}$	$6.7~\mu mol~L^{-1}$	38
MoS ₂ -rGO-PB	0.1	$2883.5 \ \mu A/\mu Mcm^{-2}$	0.3 μM- 1.15 mM	0.14 μΜ	39
Pd/MoS ₂ -IL-OMC	-0.53	$150.1 \ \mu A \ \mu M^{-1} \ cm^{-2}$	$0.020~\mu M{-}10~\mu M$	8.0 nM	40

IV. Conclusions

This study describes the use of MoS₂ films as an alternative electrode material for the fabrication of sensors. We have shown that the MoS₂ films and needles behaved as catalytically active sensors for electrochemical non-enzymatic reduction of H₂O₂. Nanorod-like MoS₂ nanostructures formed at 0.25 Jcm⁻² exhibited a large specific surface area and demonstrated accelerated direct electron transfer between the modified electrode surfaces. The resultant electrochemical sensor showed high detection sensitivity and good selectivity towards H₂O₂ sensing. The LOD for H₂O₂ observed in this study coincides with the typical levels of H₂O₂ in physiological systems. The capability of laser irradiation to prepare MoS₂ needles holds significant potential for use in the adsorption of toxic gases, dyes, and heavy metal ions as well as other environmental applications.

Acknowledgments

The authors would like to acknowledge support from National Science Foundation awards #1836767 and #2029974. We appreciate the help of Bella Ruiz, an undergraduate student, for assistance with the schematic figure.

Conflict of interest statement

On behalf of all authors, the corresponding author states that there is no conflict of interest.

Data availability

The datasets generated during and/or analyzed during the current study are available from the corresponding author on reasonable request.

References

- 1. R. Yan, J.R. Simpson, S. Bertolazzi, J. Brivio, M. Watson, X. Wu, A. Kis, T. Luo, A.R. Hight Walker, H.G. Xing, ACS nano 8, 986-993 (2014).
- 2. D. Xiao, G. Liu, W. Feng, X. Xu, W. Yao, Phys. Rev. Lett. 108, 196802 (2012).
- 3. S. Nagata, T. Aochi, T. Abe, S. Ebisu, T. Hagino, Y. Seki, K. Tsutsumi, J. Phys. Chem. Solids 53, 1259-1263 (1992).
- 4. K. Kang, S. Xie, L. Huang, Y. Han, P.Y. Huang, K.F. Mak, C. Kim, D. Muller, J. Park, Nature 520, 656-660 (2015).
- 5. J. Feng, K. Liu, M. Graf, M. Lihter, R.D. Bulushev, D. Dumcenco, D.T. Alexander, D. Krasnozhon, T. Vuletic, A. Kis, Nano Lett. 15, 3431-3438 (2015).
- 6. M. Calandra, Nature Nanotechnol. 10, 737-738 (2015).
- 7. S. Manzeli, D. Ovchinnikov, D. Pasquier, O.V. Yazyev, A. Kis, Nature Rev. Mater. 2, 1-15 (2017).
- 8. B. Radisavljevic, A. Radenovic, J. Brivio, V. Giacometti, A. Kis, Nature Nanotechnol. 6, 147-150 (2011).
- 9. H.M. Hill, A.F. Rigosi, K.T. Rim, G.W. Flynn, T.F. Heinz, Nano Lett. 16, 4831-4837 (2016).
- 10. RM. Trujillo, DE. Barraza, ML. Zamora, A. Cattani-Scholz, RE. Madrid. Sensors (Basel), 21(6), 2204 (2021).
- 11. Y. Zhan, Z. Liu, S. Najmaei, P.M. Ajayan, J. Lou, Small 8, 966-971 (2012).
- K. Liu, W. Zhang, Y. Lee, Y. Lin, M. Chang, C. Su, C. Chang, H. Li, Y. Shi, H. Zhang, Nano Lett. 12, 1538-1544
 (2012).
- 13. Y. Lee, X. Zhang, W. Zhang, M. Chang, C. Lin, K. Chang, Y. Yu, J.T. Wang, C. Chang, L. Li, Adv. Mater. 24, 2320-2325 (2012).
- S. Najmaei, Z. Liu, W. Zhou, X. Zou, G. Shi, S. Lei, B.I. Yakobson, J. Idrobo, P.M. Ajayan, J. Lou, Nature Mater. 12, 754-759 (2013).
- D. Dumcenco, D. Ovchinnikov, K. Marinov, P. Lazic, M. Gibertini, N. Marzari, O.L. Sanchez, Y. Kung, D. Krasnozhon, M. Chen, ACS nano 9, 4611-4620 (2015).
- 16. J. Narayan, A.R. Srivatsa, M. Peters, S. Yokota, K.V. Ravi, Appl. Phys. Lett. 53, 1823-1825 (1988).

- 17. L. Zeng, NE Richey, DW Palm, IK. Oh, J. Shi, C. Maclsaac, T. Jaramillo, SF Bent. Journal of Vacuum Science & Technology A: Vacuum, Surfaces, and Films.38(6):060403 (2020).
- 18. P. Joshi, S. Shukla, S. Gupta, P.R. Riley, J. Narayan, R. Narayan, ACS Appl. Mater. Interfaces 14, 37149-37160 (2022).
- 19. P.C. Pandey, S. Shukla, Y. Pandey, RSC Adv. 6, 80549-80556 (2016).
- 20. Y. Shu, W. Zhang, X. Yin, L. Zhang, Y. Yang, D. Ma, Q. Gao, J. Colloid Interface Sci. 566, 248-256 (2020).
- 21. W. Zhang, C. Wang, L. Guan, M. Peng, K. Li, Y. Lin, J. Mater. Chem. B 7, 7704-7712 (2019).
- 22. D. Li, X. Liu, R. Yi, J. Zhang, Z. Su, G. Wei, Inorg. Chem. Front. 5, 112-119 (2018).
- 23. D. Lin, Y. Li, P. Zhang, W. Zhang, J. Ding, J. Li, G. Wei, Z. Su, RSC Adv. 6, 52739-52745 (2016).
- 24. M. Pavličková, L. Lorencová, M. Hatala, et al. Sci Rep 12, 11900 (2022).
- 25. A. Sinha, B. Tan, Y. Huang, H. Zhao, X. Dang, J. Chen, R. Jain, Trends in Analytical Chemistry 102:75-90 (2018).
- 26. S. Kanaparthi, SG. Singh. ACS Sustainable Chemistry & Engineering. 26;9(44):14735-43 (2021).
- 27. R.K. Singh, J. Narayan, Phys. Rev. B 41, 8843 (1990).
- 28. P. Joshi, S. Gupta, P.R. Riley, R. J. Narayan J. Narayan, J. (2021). Diamond and Related Materials, 117, 108481 (2021).
- 29. J. Zhang, D. Han, Y. Wang, L. Wang, X. Chen, X. Qiao, and X. Yu, Microchimica Acta, 187(6), 1-10 (2020).
- 30. D. Lin, Z. Su, and G. Wei, Materials today chemistry, 7, 76-83 (2018).
- 31. J.X. Zhou, L.N. Tang, F. Yang, F.X. Liang, H. Wang, Y.T. Li, and G.J. Zhang, Analyst, 142(22), 4322-4329 (2017).
- 32. K. Zhang, H. Sun, and S. Hou, Analytical Methods, 8(18), 3780-3787 (2016).
- 33. D. Lin, Y. Li, P. Zhang, W. Zhang, J. Ding, J. Li, G. Wei, and Z. Su, RSC advances, 6(58), 52739-52745 (2016).
- 34. H.U. Kim, H. Kim, C. Ahn, A. Kulkarni, M. Jeon, G.Y. Yeom, M.H. Lee, and T. Kim, RSC advances, 5(14), 10134-10138 (2015).
- 35. W. Zhang, C. Wang, L. Guan, M. Peng, K. Li, and Y. Lin, Journal of Materials Chemistry B, 7(48), 7704-7712 (2019).
- 36. L. Zhu, Y. Zhang, P. Xu, W. Wen, X. Li, and J. Xu, Biosensors and Bioelectronics, 80, 601-606 (2016).
- 37. S. Su, X. Han, Z. Lu, W. Liu, D. Zhu, J. Chao, C. Fan, L. Wang, S. Song, L. Weng, and L. Wang, ACS Applied Materials & Interfaces, 9(14), 12773-12781 (2017).

- 38. H. Liu, X. Su, C. Duan, X. Dong, and Z. Zhu, Materials Letters, 122, 182-185 (2014).
- 39. Z. Cheng, Q. Shen, H. Yu, D. Han, F. Zhong, and Y. Yang, Microchimica Acta, 184(12), 4587-4595 (2017).
- 40. B. Xu, L. Yang, F. Zhao, and B. Zeng, Electrochimica Acta, 247, 657-665 (2017).

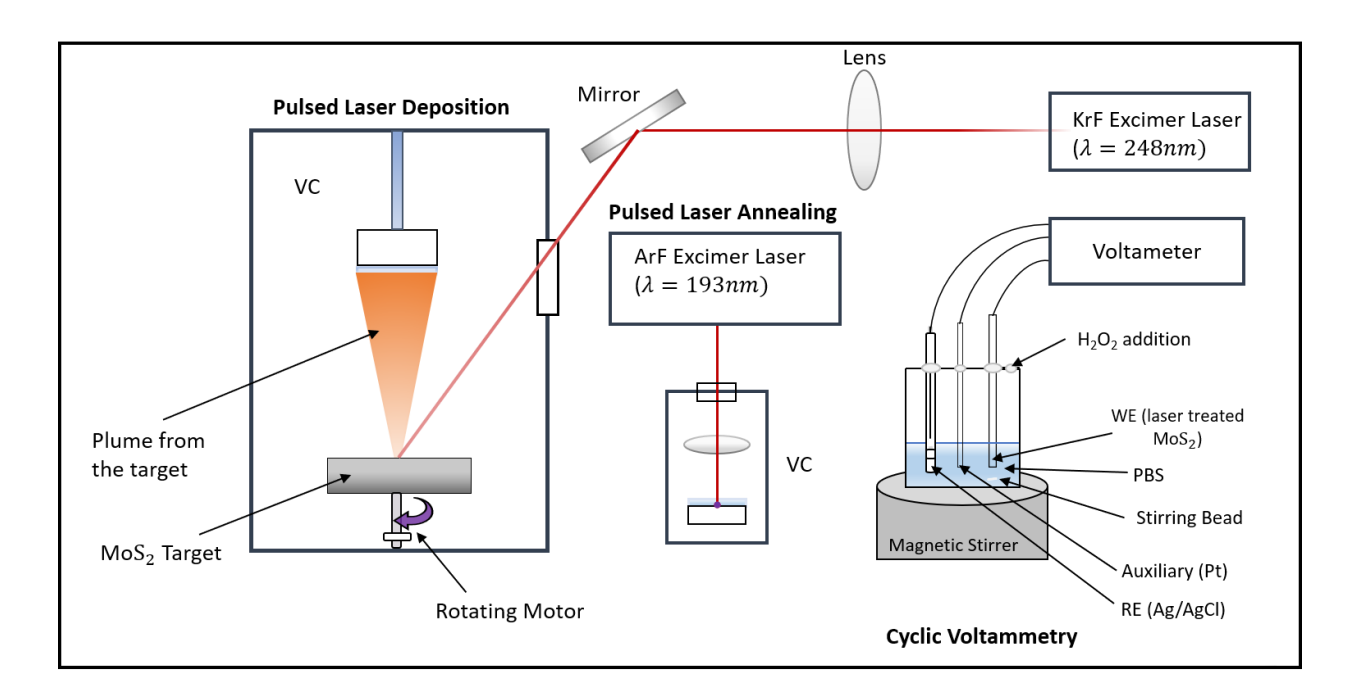


Fig. 1. Schematic describing the synthesis of MoS₂-coated silicon working electrode for the electrochemical sensing of hydrogen peroxide (H₂O₂); synthesis involves depositing and irradiating MoS₂ thin films with an excimer laser inside a vacuum chamber (VC).

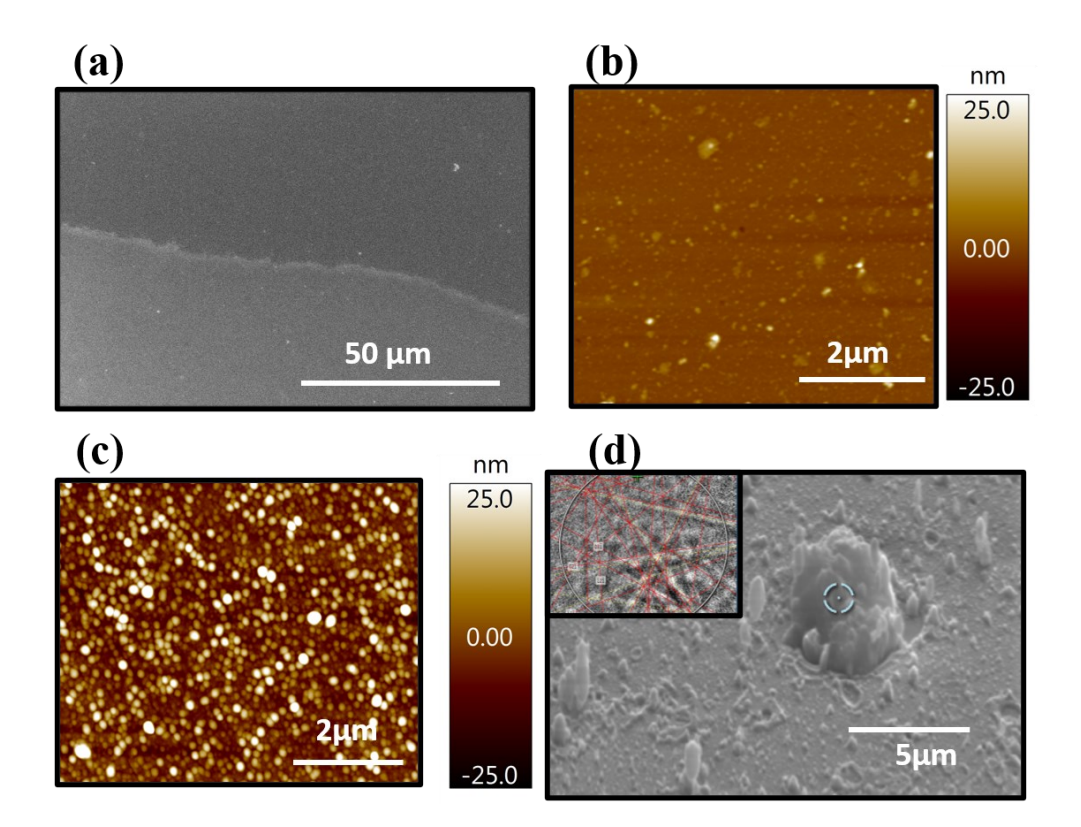


Fig. 2. (a) SEM micrograph MoS_2 thin film depicting the sharp laser annealed and non-annealed interface on <111> Si substrate; (b) 2D AFM image of laser annealed MoS_2 at 0.08 Jcm⁻²; (c, d) 2D AFM and SEM image of laser annealed MoS_2 at 0.25 Jcm⁻² (inset to (d) shows the EBSD pattern of MoS_2 needles).

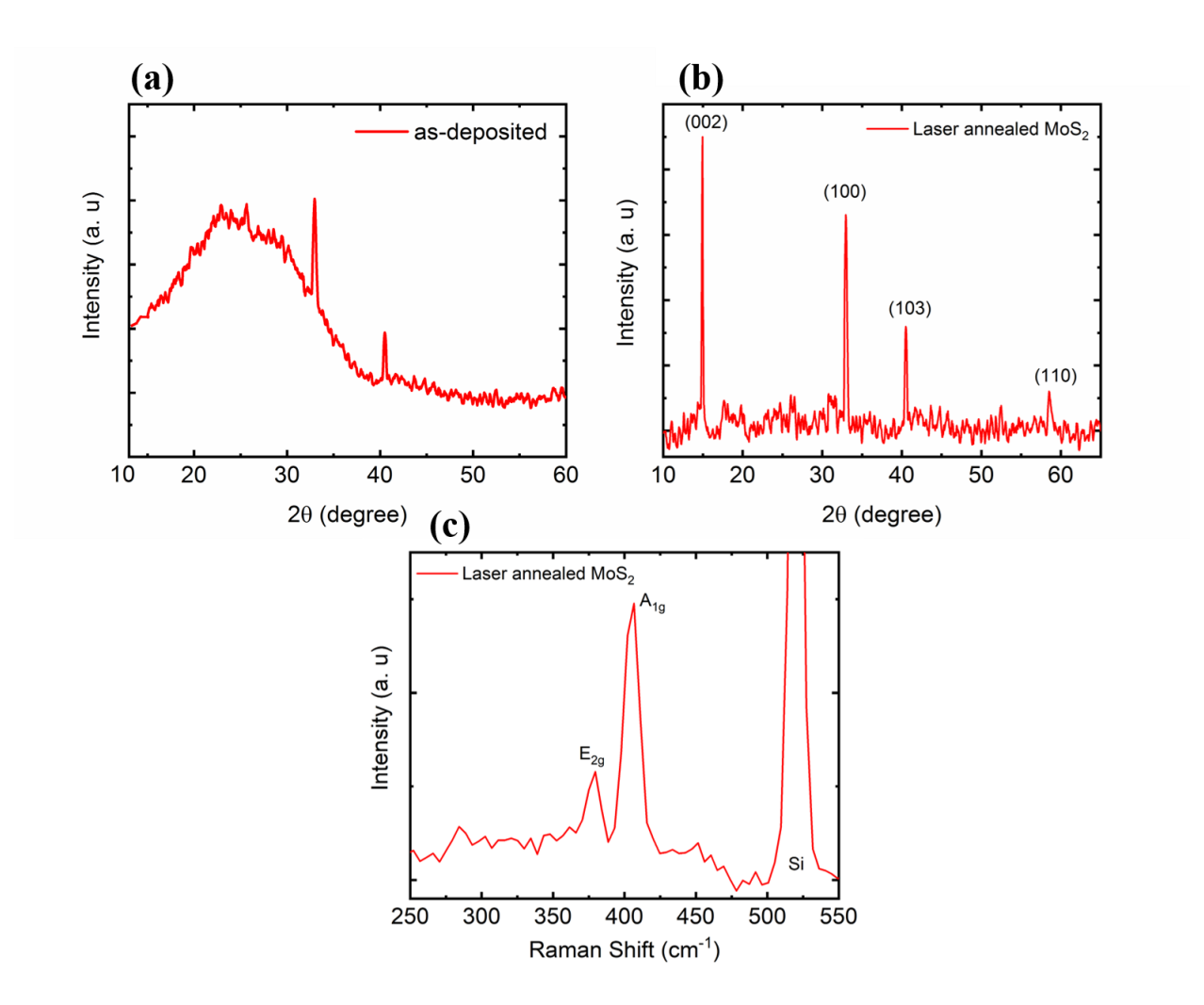


Fig. 3. (a, b) XRD before and after laser annealing of MoS2 at 0.08 Jcm⁻², (c) Raman spectrum of MoS2 after laser annealing at 0.1 Jcm⁻².

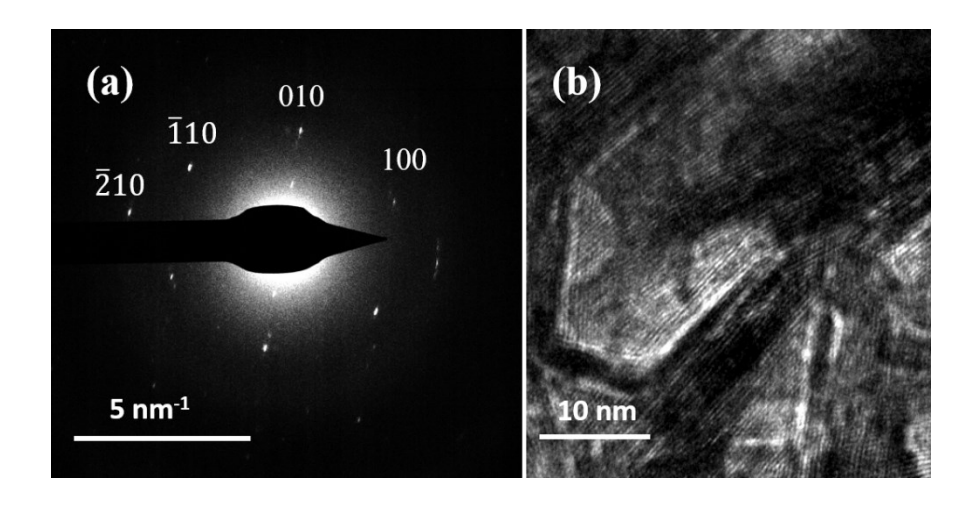


Fig. 4. (a) SAED pattern of MoS₂ along [001] zone axes, (b) TEM micrograph of laser annealed MoS₂ showcasing the lattice fringes (0.08 Jcm⁻²).

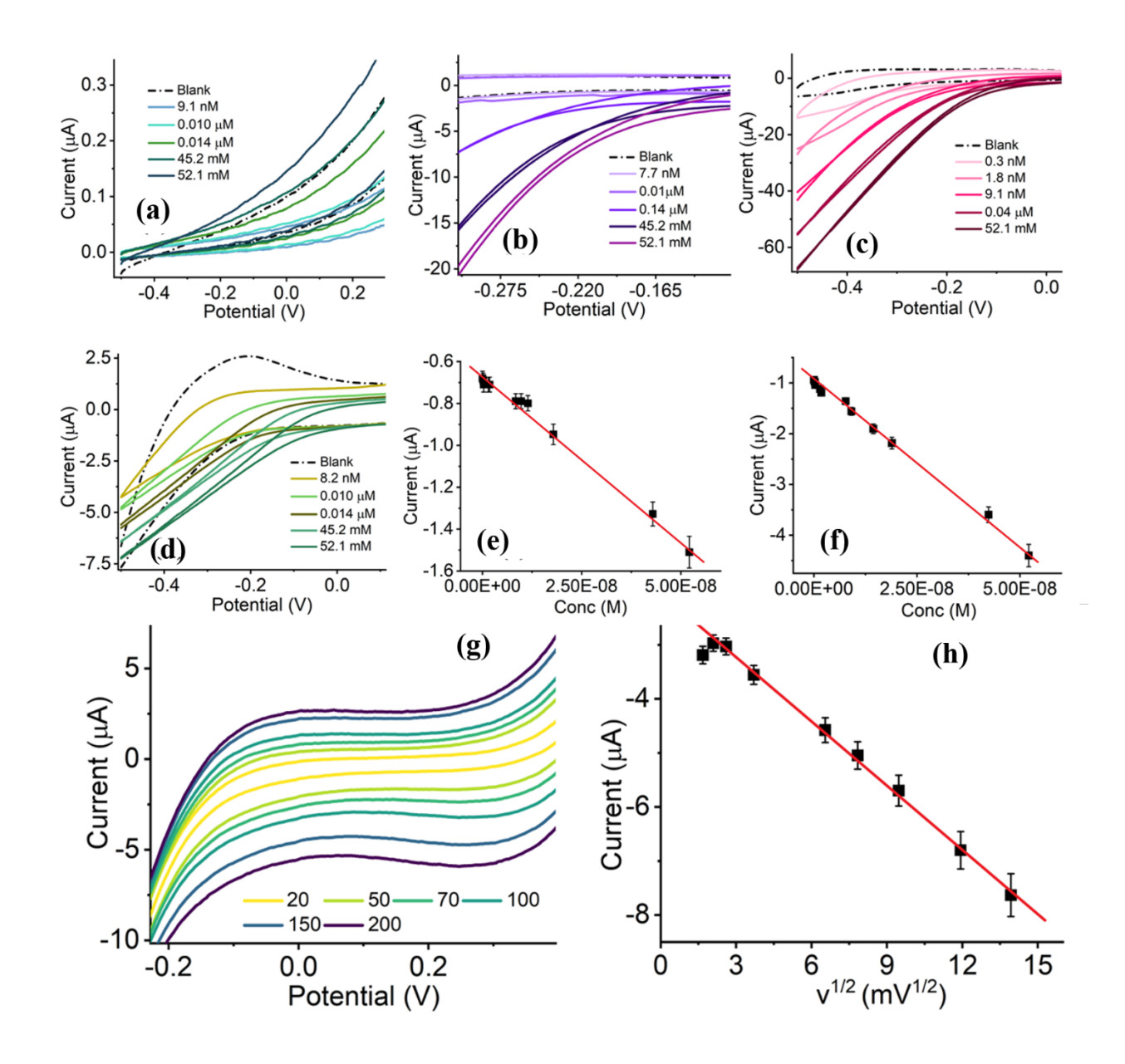


Fig. 5. CV curves for MoS_2 nanofilms (a) as deposited (E₁), (b) E₂, (c) E₃, and (d) E₄; corresponding calibration plots I_p vs. conc. for (e) E₂ and (f) E₃; (g) CV curves at different scan rates for E₃; and (h) scan rate vs. i_p for E₃.